

Parametric Mössbauer radiation source

O. D. Skoromnik,^{1,*} I. D. Feranchuk,^{2,3,4,†} J. Evers,¹ and C. H. Keitel¹

¹Max Planck Institute for Nuclear Physics, Saupfercheckweg 1, 69117 Heidelberg, Germany

²Atomic Molecular and Optical Physics Research Group,

Advanced Institute of Materials Science, Ton Duc Thang University,

19 Nguyen Huu Tho Str., Tan Phong Ward, District 7, Ho Chi Minh City, Vietnam

³Faculty of Applied Sciences, Ton Duc Thang University, 19 Nguyen Huu Tho Str.,
Tan Phong Ward, District 7, Ho Chi Minh City, Vietnam

⁴Belarusian State University, 4 Nezavisimosty Ave., 220030, Minsk, Belarus

Numerous applications of Mössbauer spectroscopy^{1–3} are related to a unique resolution of absorption spectra of resonant radiation in crystals, when the nucleus absorbs a photon without a recoil. However, the narrow nuclear linewidth renders efficient driving of the nuclei challenging, restricting precision spectroscopy^{4,5}, nuclear inelastic scattering⁶ and nuclear quantum optics^{7–9}. Moreover, the need for dedicated X-ray optics^{2,10} restricts access to only few isotopes, impeding precision spectroscopy of a wider class of systems. Here, we put forward a novel Mössbauer source, which offers a high resonant photon flux for a large variety of Mössbauer isotopes, based on relativistic electrons moving through a crystal and emitting parametric Mössbauer radiation essentially unattenuated by electronic absorption. As a result, a collimated beam of resonant photons is formed, without the need for additional monochromatization. We envision the extension of high-precision Mössbauer spectroscopy to a wide range of isotopes at accelerator facilities using dumped electron beams.

Keywords: Mössbauer spectroscopy, X-ray sources, Parametric X-ray radiation (PXR), Parametric Mössbauer radiation (PMR), Extremely asymmetric diffraction

Traditional Mössbauer spectroscopy uses radioactive sources, which provide essentially background-free near-resonant γ -radiation with a spectral width of order of the natural linewidth of the involved nuclear transitions^{1–3}. Accelerator-based X-ray sources offer orders of magnitude more resonant photon flux, but the short X-ray pulses contain an intense off-resonant background, which strongly exceeds the resonant component. As a result, Mössbauer spectroscopy usually is performed in the time domain^{3,11}, removing the “prompt” non-resonant background via temporal gating of the detectors. This, for instance, restricts the study of short-lived isotopes, for which the gating leads to a severe loss of signal photons due to the fast initial decay.

Alternatively, synchrotron Mössbauer sources (SMS)^{12–16} can be employed to monochromatize the synchrotron radiation to few natural linewidths using pure nuclear Bragg reflexes, enabled by the suppression of electronic reflections via particular crystal symmetries. In addition, usually a specific Mössbauer isotope is targeted, requiring dedicated X-ray optics such as monochromators to reduce the off-resonant background component. Therefore, it is challenging to make new Mössbauer isotopes accessible at modern pulsed X-ray sources, which hinders the exploration of new scientific applications of specific Mössbauer nuclei^{2,10}.

An alternative scheme to generate X-rays is parametric X-ray radiation (PXR), based on relativistic electrons moving through a crystal^{17–22}. In PXR, the electron self-field diffracts on the crystallographic planes, which leads to the generation of electromagnetic radiation. Its relative spectral and angular widths are suppressed by the large electron energy E , via the relativistic γ factor $\gamma = E/m_e c^2$, resulting in quasi-monochromatic and well collimated PXR radiation. Moreover, it is possible to fix the electron angle of incidence in

such a way that one of the PXR peaks is in resonance with a nuclear Mössbauer transition, giving rise to Parametric Mössbauer Radiation (PMR)²³.

However, conventional PXR schemes are limited in intensity due to substantial X-ray absorption in the crystal^{23,24}. This can be understood by noting that the PXR intensity depends on the crystal polarizability^{17,19}. For crystal diffraction, the polarizability is maximized near the resonance frequencies, where also the absorption becomes large. To overcome this issue, a particular geometry featuring extremely asymmetric diffraction (EAD) was suggested²⁵. This geometry exploits a peculiar PXR feature, namely, that the radiation is emitted under a large angle relative to the electron velocity, which is in stark contrast with other mechanisms generating radiation from relativistic particles. In the EAD geometry, the electrons are moving in a thin crystal layer parallel to the crystal-vacuum interface in such a way that the emitted photons immediately exit the crystal without much absorption. This effectively increases the intensity of the radiation by two orders of magnitude with respect to the conventional transition geometries. However, such EAD geometries have not been studied in the case of PMR.

Here, we put forward a novel versatile source for Mössbauer spectroscopy, which is based on PXR simultaneously satisfying the Mössbauer resonance condition to effectively excite the nuclei and the EAD condition to suppress absorption. This source offers a competitive nuclear resonant photon flux for a large variety of Mössbauer crystals. In addition, for certain crystals the SMS crystal symmetry condition can be fulfilled leading to the suppression of the off-resonant electronic background radiation. In this case, our calculations predict almost background-free emission of Mössbauer radiation, paving the way to Mössbauer spectroscopy on short-lived iso-

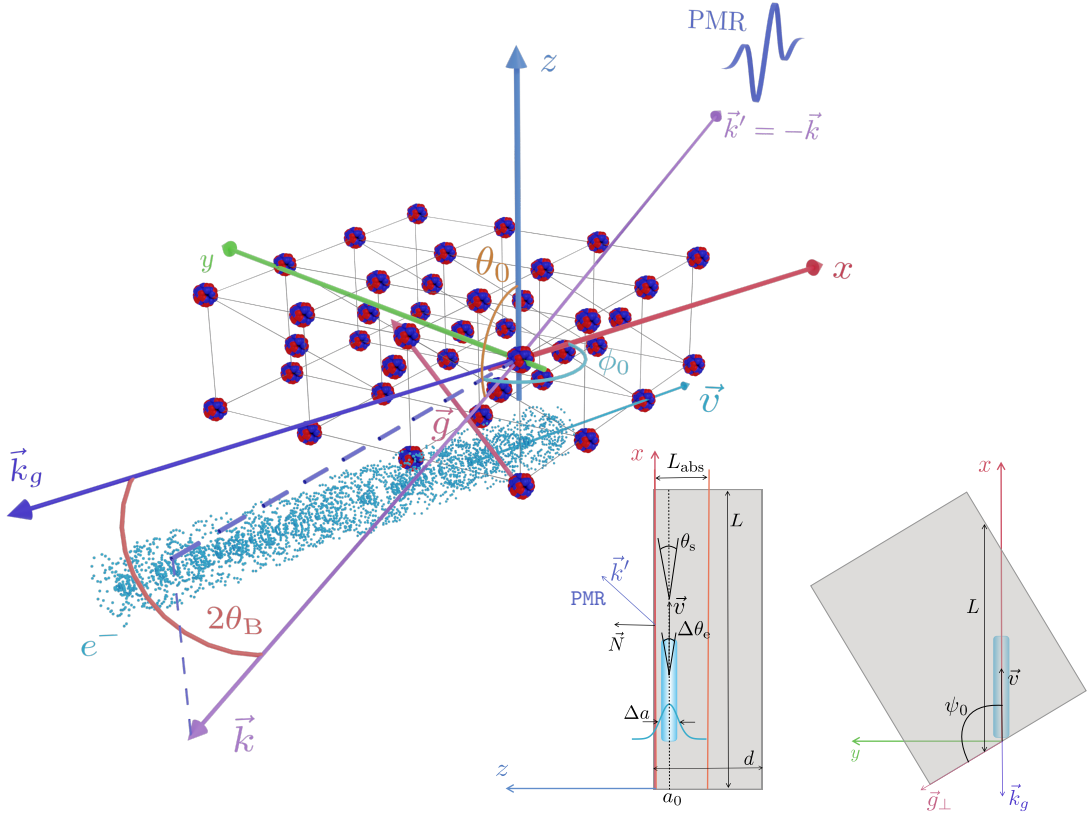


Figure 1. **Schematic setup of the PMR generation.** The electron bunch moves uniformly with velocity \mathbf{v} in the x direction. The crystal surface lies in the $x - y$ plane. \mathbf{g} is the reciprocal crystal lattice vector. PMR will be mainly emitted in the direction given by the vector $\mathbf{k}' = -\mathbf{k} = -k_0(\sin \theta_0 \cos \phi_0, \sin \theta_0 \sin \phi_0, \cos \theta_0)$, and thus rapidly leaves the crystal without significant electronic absorption. $\mathbf{k}_g = \mathbf{k} + \mathbf{g}$ and θ_B is the Bragg angle. The energy of the PXR is tuned using the angle ψ_0 between the electron velocity and the projection \mathbf{g}_\perp of \mathbf{g} on the crystal surface. The resonance condition is $k^2 = (\omega_0/c)^2 = k_0^2$, which yields $\cos \psi_0 = -v/(k_0 c) \times (k_0^2 \gamma^{-2} + g^2)/(2\sqrt{g^2 - g_z^2})$.

topes directly in the energy domain, without the need for additional time gating or the development of dedicated monochromatizers.

We illustrate our approach in the case of ^{121}Sb , for which our simulations predict about 10^3 resonant photons per second and nuclear linewidth, essentially background-free. We further discuss two isotopes without the SMS condition: ^{133}Cs in order to illustrate the interplay between the electron and nuclear components of the crystal polarizabilities, and ^{57}Fe as the classical workhorse of Mössbauer spectroscopy. In the latter case, more than 10^4 photons per second and natural linewidth Γ are predicted. The total linewidth of a PMR source is $\sim 5 - 20 \Gamma$ depending on the crystal.

In order to calculate PXR and PMR (see Methods for details on the calculation), we solve the inhomogeneous Maxwell's equations using a Green's function and the standard two-wave approximation approach of dynamical diffraction theory²⁶. We find that the wave vector $\mathbf{k}' = -\mathbf{k}$ corresponding to the maximum PXR emission is determined as a solution of two equations: (a) the Cherenkov radiation condition¹⁸

$$q' = \text{Re } q = 1 + \frac{(\mathbf{k} + \mathbf{g}) \cdot \mathbf{v}}{\omega_0} = 0 \quad (1)$$

for the diffracted wave and (b) minimal value for the deviation from Wulff-Bragg's condition¹⁷⁻¹⁹

$$|\alpha_B| = \frac{|(\mathbf{k} + \mathbf{g})^2 - k^2|}{|\mathbf{k}|^2} = \frac{|2\mathbf{k} \cdot \mathbf{g} + g^2|}{|\mathbf{k}|^2} \quad (2)$$

The latter condition describes the diffraction of an electron self-field on the crystallographic planes with the reciprocal lattice vector $\mathbf{g} = (g_x, g_y, g_z)$, where \mathbf{v} is the electron velocity and $|\mathbf{k}| = \omega_0/c$ with ω_0 the frequency of the resonant Mössbauer transition.

Next, we consider the EAD geometry case^{25,27}, see Fig. 1, in which electrons are moving parallel to the crystal-vacuum interface (parallel to $x - y$ plane) and emit radiation under a large angle to the crystal surface. In this geometry, the angle ψ_0 between \mathbf{g}_\perp and the electron velocity \mathbf{v} we adjust in such a way that the frequency of the emitted radiation is coincident with the resonance frequency of the Mössbauer isotope.

Solving Eqs. (1)-(2) under the condition $\mathbf{k}_g \cdot \mathbf{N} = (\mathbf{k} + \mathbf{g}) \cdot \mathbf{N} = 0$, which specifies the EAD geometry, we find that the maximum of the X-ray emission is in the direction $\mathbf{k}' = -\mathbf{k} = (g_x + \omega_0/v, g_y, g_z)$. The z component causes the generated radiation to immediately leave the crystal, such that absorption within the crystal is greatly reduced.

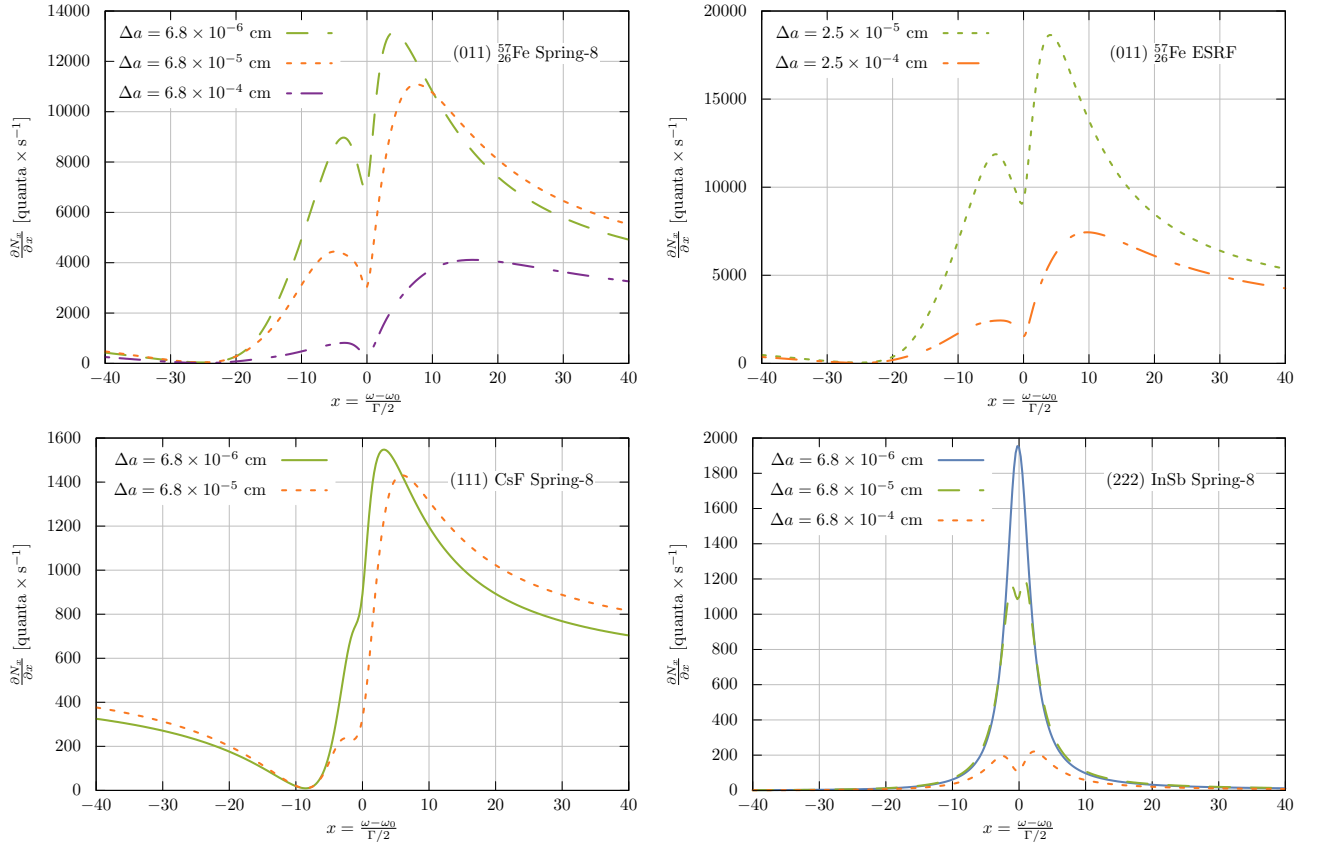


Figure 2. **Emission spectra of the PMR source.** The figure shows the number of emitted X-ray photons per second as a function of the dimensionless frequency $x = (\omega - \omega_0)/(\Gamma/2)$. The results are averaged over the electron beam parameter distributions, for different transversal widths and divergences of the electron bunch, keeping the emittance constant. The top row compares the (011) reflection of an α -iron crystal for Spring-8 and ESRF electron beam parameters. The bottom left panel shows the emission from the (111) reflection of the CsF crystal, with Spring-8 electron parameters. The bottom right panel shows pure PMR emission from the (222) reflection of the InSb crystal. For all panels, we assume an angular spread in the y direction of 10^{-3} rad. The crystal lengths are chosen as $L = 0.5$ cm (Spring-8) and $L = 0.2$ cm (ESRF), respectively. At Spring-8, the electron energy is $E = 8000$ MeV, the vertical emittance is $\epsilon = 6.8 \times 10^{-10}$ cm-rad, the vertical beam size is $\Delta a = 6 \times 10^{-4}$ cm, and the electron current is $j = 100$ mA. At ESRF, the corresponding parameters are $E = 6030$ MeV, $\epsilon = 2.5 \times 10^{-9}$ cm-rad, $\Delta a = 7.9 \times 10^{-4}$ cm, and $j = 200$ mA.

Next, we insert the solution of the diffraction problem for the electric field in the standard expression for the energy density of the emitted radiation and integrate over the particle trajectory and over the X-ray spherical emission angle ϕ . This yields the spectral-angular distribution of the emitted photons

$$\frac{\partial^2 N}{\partial \omega \partial \theta} = \frac{e_0^2}{4\pi\hbar c \omega} \frac{1}{|\sin \phi_0|} \sum_{s=\sigma,\pi} \left(|E_{g1s}|^2 \left(\frac{\mathbf{v} \cdot \mathbf{e}_{1s}}{c} \right)^2 \times \frac{1 - e^{-2k_0 L q_s''}}{q_s''} e^{-2k_0 |z_0 \epsilon_{1s}''|} \right), \quad (3)$$

where L is the crystal length, z_0 is the electron initial coordinate, and $E_{g1s} = c_s \chi_g / (\alpha_B + \chi_0)$ is the amplitude of the diffracted wave. The index s sums over the σ and π polarizations, with $c_\sigma = 1$ and $c_\pi = \cos 2\theta_B$, and polarization vectors $\mathbf{e}_{1\sigma} = \mathbf{k} \times \mathbf{g} / |\mathbf{k} \times \mathbf{g}|$ and $\mathbf{e}_{1\pi} = \mathbf{k}_g \times \mathbf{e}_{1\sigma} / |\mathbf{k}_g \times \mathbf{e}_{1\sigma}|$. Finally, $q_s'' = |\theta_{ez} \epsilon_{1s}''|$, where θ_{ez} characterizes the z -component of the electron velocity, and ϵ_{1s}'' is the imaginary part of the

solution of the dispersion equation²⁷ for the fields in a crystal $\epsilon_{1s} = -\chi_0 / (2 \cos \theta_0) + c_s^2 \chi_g \chi_{-g} / [2(\alpha_B + \chi_0) \cos \theta_0]$.

This expression contains two key quantities, which determine PMR and PXR, namely, the dielectric susceptibilities $\chi_0(\omega) = \chi_{0e}(\omega_0) + \chi_{0n}(\omega)$ and $\chi_g(\omega) = \chi_{ge}(\omega_0) + \chi_{gn}(\omega)$. They each comprise an electronic (χ_{0e}, χ_{ge}) and a nuclear (χ_{0n}, χ_{gn}) contribution, and PMR becomes sizable, if the parameter $\xi = |\chi_n(\omega_0) / \chi_e(\omega_0)| > 1$. The nuclear part

$$\chi_{gn}(\omega) = -\frac{4\pi}{\omega_0^2 c^3} \frac{S(\mathbf{g})}{V} \frac{\eta e^{-W(\mathbf{k}, \mathbf{k}_g)}}{\omega_0(1 + \alpha_c)} \frac{\Gamma/2}{(\omega - \omega_0) + i\Gamma/2} \quad (4)$$

has a resonance character^{1,28} and is responsible for the PMR. Here, $S(\mathbf{g})$ is the structure factor, $e^{-W(\mathbf{k}, \mathbf{k}_g)}$ the Debye-Waller factor, V the volume of the unit cell, α_c the coefficient of the internal conversion and Γ the natural line width of the transition.

For our numerical analysis, we choose electron beam parameters from the Spring-8²⁹ and ESRF³⁰ storage ring facil-

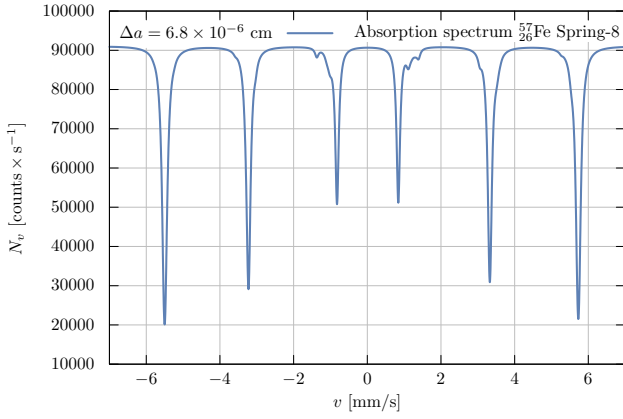


Figure 3. **Example absorption spectrum.** An absorption spectrum simulated with the PMR predicted for the Spring-8 experimental facility with $\Delta a = 6.8 \times 10^{-6}$ cm. As a target, a non-enriched ($\eta = 0.02$) α -iron crystal of thickness $D = 5 \mu\text{m}$ is assumed. The contrast is determined via the ratio of the electron and the nuclear contributions into the crystal polarizability near the resonance frequency and in the case of α -iron ~ 20 .

ities, where we consider the possibility to focus the electron beams to smaller electron beam diameters Δa .

We investigated the emission from three crystals with cubic lattices. The first two are without the SMS condition: the α -iron crystal, enriched to 90% in the resonant Mössbauer isotope ^{57}Fe and the CsF crystal, which contains ^{133}Cs . The third crystal — the InSb crystal contains the resonant isotope ^{121}Sb — that is especially interesting since the two constituent atoms have similar charges, which allows one to specify a Bragg reflection for which the structure factors of Sb and In have equal magnitude but opposite sign, like in the SMS case. This significantly lowers PXR and provides a handle to achieve essentially background-free PMR.

Figure 2 shows our main results, i.e. the emission spectra as a function of the dimensionless frequency x , measured in $\Gamma/2$. Qualitatively, as expected from Eqs. (1), (2), we find that the peak of the emission occurs at frequencies where the Cherenkov radiation condition is exactly fulfilled, i.e. $q' = 0$ and the maximum of the amplitude of the diffracted wave is reached ($|\alpha_B + \chi'_0|$ is minimal). The asymmetry of the distribution is caused by the fact that the contribution of the nuclear polarizability to χ'_0 changes its sign when ω crosses the nuclear resonance frequency ω_0 .

Quantitatively, for electron bunches narrow in the transversal z -direction ($\Delta a = 6.8 \cdot 10^{-6}$ cm for Spring-8 and $\Delta a = 2.5 \cdot 10^{-5}$ cm for ESRF), our analysis predicts that the number of photons that are emitted in the spectral interval Γ ($\Delta x = 2$ in Fig. 2) near the maximum of the distribution is $N_{\text{Spring-8}}^{\text{Fe}} = 26157$ cps and $N_{\text{ESRF}}^{\text{Fe}} = 36978$ cps. For the CsF crystal, the corresponding number of photons is lower, $N_{\text{Spring-8}}^{\text{CsF}} = 3074$ cps. The reason is that the value of the ξ parameter is smaller in this case. Finally, in the case of the InSb crystal, one obtains $N_{\text{Spring-8}}^{\text{InSb}} = 3671$ cps. As expected, we find that the electronic component is strongly suppressed

due to the choice of (222) reflection, when the structure factors of In and Sb are of an opposite sign. As a result, the PMR paves the way for an essentially background-free direct spectroscopy of Sb in the energy domain.

To illustrate its capabilities, in Fig. 3 we simulate the spectroscopy of α -iron with our source. We find that a well-resolved spectrum with good contrast can be achieved.

In summary, we have suggested a versatile X-ray source for Mössbauer spectroscopy, based on Parametric Mössbauer radiation (PMR) emitted by relativistic electrons passing through a crystal. It complements currently existing Mössbauer radiation sources due to its different qualitative properties. First, the possibility to obtain collimated photon beams without the need of X-ray optics and preliminary monochromatization of the radiation. Second, this type of source is universal and can be realized for a large variety of Mössbauer crystals, including those with forbidden Bragg reflexes, thus leading to almost background free Mössbauer radiation. It therefore provides a route towards the exploration of Mössbauer spectroscopy beyond the standard isotopes. An interesting perspective is parasitic operation using dumped electron beams, since PMR converts the relativistic electrons into resonant X-ray radiation in a cm-scale crystal.

Acknowledgments

ODS is grateful to K. P. Heeg, A. Angioi, B. Nickerson, S. Kobzak, S. Bragin and D. Bakucz Canário for useful discussions.

Author contributions

ODS and IDF initially conceived the project and performed calculations. ODS generated the figures. JE proposed the averaging procedure over the electron parameters, which vary over the crystal length and contributed to the discussion about angular spread of the X-rays. ODS, IDF and JE wrote the manuscript. CHK supervised the project. All authors contributed to the preparation of the manuscript.

APPENDIX A. DETAILS OF THE CALCULATIONS

Solution of Maxwell's equations. The differential number of photons $\partial N_{\omega s} / (\partial \omega \partial \Omega)$ emitted in the frequency interval $(\omega, \omega + d\omega)$ and in the solid angle $d\Omega$ is computed in the following way^{17,18,27}. One starts from inhomogeneous Maxwell's equations for the Fourier component of the fields, which contain the current generated by a charged particle. In the case of PXR, the charged particle moves uniformly, i.e., $\mathbf{r}(t) = \mathbf{r}_0 + \mathbf{v}t$, where \mathbf{r}_0 is the initial position at $t = 0$. The displacement field $\mathbf{D}(\mathbf{r}, \omega)$ is related to the electric field $\mathbf{E}(\mathbf{r}, \omega)$ through the permittivity tensor $\epsilon_{\alpha\beta}(\mathbf{r}, \mathbf{r}_1, \omega)$, which is defined in the whole space, but has different expressions inside the crystal and outside, in vacuum. To facilitate the calculation, we expand the permittivity inside the crystal in a series over the reciprocal lattice vectors \mathbf{g} .

After this, Green's function for Maxwell's equations is defined and expressed through the solution $\mathbf{E}_{\mathbf{k}'s}^{(-)}$ of homogeneous Maxwell's equations. Then, Green's function is used to deter-

mine the field generated by the current. This field is then used in the standard expression for the energy density yielding

$$\frac{\partial^2 N_{n,\omega s}}{\partial \omega \partial \Omega} = \frac{e_0^2 \omega}{4\pi^2 \hbar c^3} \left| \int \mathbf{E}_{k's}^{(-)*}(\mathbf{r}(t), \omega) \cdot \mathbf{v}(t) e^{i\omega t} dt \right|^2, \quad (5)$$

where $\mathbf{k}' = k\mathbf{r}/r$. It is important to note that the solution $\mathbf{E}_{k's}^{(-)}$ of homogeneous Maxwell's equations possesses an asymptotic behaviour for large $|r|$ as a plane wave and an ingoing spherical wave. In contrast, when an external electromagnetic field $\mathbf{E}_{k's}^{(+)}$ is diffracted or scattered on a crystal, it has an asymptotic behavior of a plane wave and an outgoing spherical wave. However, these two field configurations are related to each other by the reciprocity theorem³¹ $\mathbf{E}_{k's}^{(-)} = \mathbf{E}_{-k's}^{(+)}$. Thus the actual problem is reduced to the solution of the diffraction problem to find the field $\mathbf{E}_{k's}^{(+)}$, the usage of the reciprocity theorem, and the subsequent application of Eq. (5). For this reason, the actual vector of the emitted photon \mathbf{k}' is related to the vector \mathbf{k} of the diffraction problem via $\mathbf{k}' = -\mathbf{k}$.

Solution of the diffraction problem. The diffraction problem is solved within the two-wave approximation of the dynamical diffraction theory²⁶, which is valid if two strong electromagnetic waves are excited in the crystal. The amplitudes of these waves satisfy a set of homogeneous algebraic equations

$$\begin{aligned} \left(\frac{k^2}{k_0^2} - 1 - \chi_0 \right) E_{k_s} - c_s \chi_{-g} E_{k_{g,s}} &= 0, \\ \left(\frac{k_g^2}{k_0^2} - 1 - \chi_0 \right) E_{k_{g,s}} - c_s \chi_g E_{k_s} &= 0, \end{aligned} \quad (6)$$

where $k_0 = \omega/c$, the incident wave $\mathbf{E}_{k_s}^{(+)} = \mathbf{e}_s E_{k_s}$ and the diffracted wave $\mathbf{E}_{k_{g,s}}^{(+)} = \mathbf{e}_{1s} E_{k_{g,s}}$. A non-trivial solution of this linear homogeneous equation system exists, if the corresponding determinant is vanishing. This condition determines the dispersion relation, and its solutions ε_{1s} and ε_{2s} fix the wave vectors $\mathbf{k}_{1,2s} = k_0 \mathbf{n} - k_0 \varepsilon_{1,2s} \mathbf{N}$ of the diffracted waves. Here, \mathbf{n} is the unit vector in the direction of the incident wave in vacuum. Having found the solutions of the dispersion equation, one writes down Maxwell's equations in the crystal and in vacuum and exploits the continuity of the fields at the crystal-vacuum interface. This fixes the amplitudes of all waves. In particular, the electromagnetic field responsible for the formation of PMR equals to $\mathbf{E}_{k_s}^{(+)} = \mathbf{e}_{1s} E_{g1s} e^{i\mathbf{k}_g \cdot \mathbf{r} - ik_0 z \varepsilon_{1s}}$, with $E_{g1s} = c_s \chi_g / (\alpha_B + \chi_0)$.

Differential number of photons emitted by an electron.

The integration over the particle trajectory in Eq. (5) with the law of motion, together with the expression $\mathbf{E}_{k_s}^{(+)}$ for the electromagnetic field yields

$$\begin{aligned} \frac{\partial^2 N_{n,\omega s}}{\partial \omega \partial \Omega} &= \frac{e_0^2 \omega}{4\pi^2 \hbar c^5} \sum_{s=\sigma,\pi} (\mathbf{e}_{1s} \cdot \mathbf{v})^2 \\ &\times \left| E_{g1s} L_g (1 - e^{-iL/L_g}) \right|^2 e^{-2k_0 |\varepsilon_{1s} z_0|}, \end{aligned} \quad (7)$$

where $L_g = 1/(k_0 q)$ is the coherence length and $q = 1 + (\mathbf{k}_g \cdot \mathbf{v})/\omega_0 - \varepsilon_{1s} v_z/c$.

In order to fix a coordinate system and to determine the direction of the X-ray emission, we for the moment consider an ideal case, in which the electron velocity does not have any component in the transverse direction and the minimum of Bragg's condition Eq. (2) is reached, i.e., $\alpha_B = \gamma^{-2}$. We align the x -axis parallel to the electron velocity, and the z -axis along the normal \mathbf{N} to the crystal surface. In this geometry, the incident electron beam, as well as the diffracted wave with vector $\mathbf{k}_g = \mathbf{k} + \mathbf{g}$, both propagate along the crystal surface²⁷, such that $\mathbf{k}_g \cdot \mathbf{N} = 0$. For a given Bragg reflex, we denote the projection of the corresponding reciprocal lattice vector \mathbf{g} onto the $x-y$ plane by \mathbf{g}_\perp .

The remaining task is to determine the deviations from the Cherenkov radiation condition $q' = \text{Re } q = 0$ and the deviation α_B from the Bragg's diffraction condition for non-ideal particle velocities. For this, we consider electrons with velocities deviating from the ideal velocity $v_0 = v\mathbf{e}_x$. We parameterize these deviations via $\mathbf{v} = v(\cos \theta \mathbf{e}_x + \theta_e)$, with $\theta_e = (0, \theta_{ey}, \theta_{ez})$ and $\theta_e^2 = \theta_{ey}^2 + \theta_{ez}^2$. Analogously, the wave vector of the emitted radiation $\mathbf{k} = k_0(\sin \theta \cos \phi, \sin \theta \sin \phi, \cos \theta)$ will acquire deviations from its ideal direction \mathbf{k}_0 . In order to determine these deviations, we expand the angular dependence in a Taylor series around the ideal direction θ_0 and ϕ_0 up to second order, i.e., $\mathbf{k} = \mathbf{k}_0 + \mathbf{u}_1 + \mathbf{u}_2$; $k^2 = k_0^2$; $\mathbf{k}_0 \cdot \mathbf{u}_1 = 0$. As a result of the deviations from the ideal directions, the quantities q' and α_B will exhibit corresponding variations

$$\begin{aligned} q' &= (\theta - \theta_0) \cos \theta_0 \cos \phi_0 - (\phi - \phi_0) \sin \theta_0 \sin \phi_0, \quad (8) \\ \alpha_B &= -\left[\gamma^{-2} + (\theta_{ez} - (\theta - \theta_0) \sin \theta_0)^2 \right. \\ &\quad \left. + (\theta_{ey} + (\phi - \phi_0) \sin \theta_0 \cos \phi_0 \right. \\ &\quad \left. + (\theta - \theta_0) \cos \theta_0 \sin \phi_0)^2 \right]. \quad (9) \end{aligned}$$

The integration over the emission angles with respect to ϕ is performed in the following manner. First, we apply a variable change $\phi - \phi_0 \rightarrow q'$. Second, we exploit the fact that the distribution function is sharply peaked near $\phi = \phi_0$, which allows us to extend the integration range from $[-\phi_0, 2\pi - \phi_0]$ to the interval $(-\infty, \infty)$. Third, since the imaginary part of q is much smaller than its real part, we can simplify its evaluation by using the value ϕ for the maximum of the intensity. This intensity maximum is located at $q' = 0$, which fixes the relation between θ and ϕ . Thus, we substitute $\phi - \phi_0 = (\theta - \theta_0) \cot \theta_0 \cot \phi_0$ in the imaginary part of q . Finally, we perform the integration with the help of the residue theorem yielding Eq. (3).

In addition, it is important to note that the electron velocity spread in the transversal y -direction, which is typically^{29,30} much larger than the corresponding spread in the z -direction, does not influence the emitted number of photons. This is due to the independence of the photon distribution function of the initial position y_0 of the electron for the case of the EAD geometry.

Averaging over the electron bunch parameters and multiple electron scattering. The velocity distribution of experimentally available electron bunches is characterized via

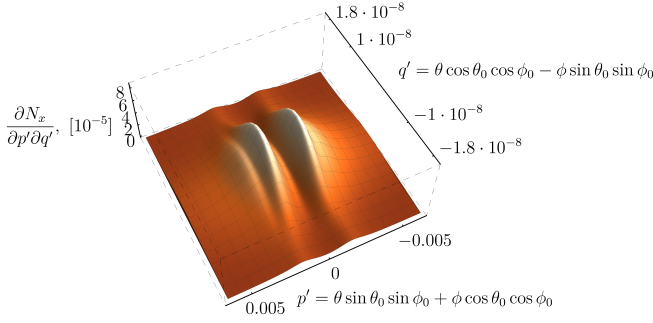


Figure 4. **Angular distribution of the PMR intensity.** The figure shows results for the Spring-8 facility as a function of $p' = \theta \sin \theta_0 \sin \phi_0 + \phi \cos \theta_0 \cos \phi_0$ and $q' = \theta \cos \theta_0 \cos \phi_0 - \phi \sin \theta_0 \sin \phi_0$ parameters for (011) reflection from α -iron crystal. When $q' = 0$, the Cherenkov radiation condition is exactly fulfilled. The angular distribution is averaged over the electron bunch characteristics with the parameters: $\Delta a = 6.8 \cdot 10^{-6}$ cm, $\Delta \theta_{ez} = 10^{-4}$ rad, $\Delta \theta_{ey} = 10^{-3}$ rad and normalized to one electron and a measurement time of one second.

the emittance $\epsilon_{y,z} = \Delta a \Delta \theta_{ey,z}$, with Δa the transversal and $\Delta \theta_{ey,z}$ the angular spreads. As a result, we need to average the spectral-angular emission distribution obtained for a single electron over the parameters of the entire electron bunch. This is achieved by convolving the emission distribution with the electron angular distribution θ_{ey} , θ_{ez} and the initial z_0 coordinate distribution. We consider Gaussian distribution functions for the electron beam parameters given by

$$G(\theta_{ez}, \theta_{ey}, z_0) = CF(\theta_{ez}, \theta_{ey}, z_0), \quad (10)$$

$$F = \exp[-((\theta_{ez} - \theta_{0e})^2 / (\theta_s^2 + \Delta \theta_{ez}^2) + \theta_{ey}^2 / (\theta_s^2 + \Delta \theta_{ey}^2))] \times \exp[-(z_0 - a_0)^2 / \Delta a^2].$$

The constant C is a normalization constant, chosen such that the total intensity corresponds to the single electron case, i.e., $\int d\theta_{ez} d\theta_{ey} dz_0 G(\theta_{ez}, \theta_{ey}, z_0) = 1$. The angle θ_{0e} is the mean incidence angle of the electron bunch on the crystal. The angle $\theta_s^2 = (E_c/E)^2 (L/L_R)$ characterizes multiple electron scattering³², with $E_c \approx 21$ MeV, L the crystal length and L_R the radiation length. For Fe, the latter is $L_R^{\text{Fe}} = 1.757$ cm³³, for CsF $L_R^{\text{CsF}} = 2.227$ cm³³ and for InSb $L_R^{\text{InSb}} = 3.701$ cm³³.

In addition, we perform the averaging over the beam transversal spread. For this we consider that the beam divergence is not constant along the crystal length, but is given by

$$\sigma(s) = \sqrt{\Delta a^2 + \epsilon^2 \frac{s^2}{\Delta a^2}}, \quad -L/2 \leq s \leq L/2 \quad (11)$$

instead. Here Δa is the transversal spread in the focus center. Therefore, in the actual calculation we vary Δa in Eq. (10) from $\sigma(-L/2)$ to $\sigma(L/2)$ in $R - 1$ steps and average the

resulting spectra over the resulting values, i.e. $\partial N_x / \partial x = 1/R \sum_{i=0}^{R-1} \partial N_x^i / \partial x$. Therefore, in all figures above the given value Δa corresponds to the value in the center of the focus of the beam.

Temperature effects. The effects of lattice vibrations on the crystal polarizabilities²⁸ due to the temperature are taken into account with the help of the Debye–Waller factor $e^{-W(k,k_g)}$, which for temperatures much smaller than the Debye temperature Θ_D and an isotropic cubic crystal is expressed as

$$W = \frac{3\hbar^2 g^2}{8mk_B \Theta_D} \left[1 + \frac{2\pi^2}{3} \left(\frac{T}{\Theta_D} \right)^2 \right], \quad (12)$$

where k_B is the Boltzmann constant, and m the mass of the resonant isotope. For α -iron the Debye temperature $\Theta_D^{\text{Fe}} = 470^\circ$ K, for CsF $\Theta_D^{\text{CsF}} = 109^\circ$ K and for InSb $\Theta_D^{\text{InSb}} = 163^\circ$ K.

Numerical values of the parameters used in the calculations. We choose the most intense reflection for the α -iron crystal, namely, the (011) reflection. For this reflection we employ the following parameters, taken from the X-ray database³⁴

$$\begin{aligned} \hbar\omega_B &= 14.41 \text{ keV}, & k_0 &= 7.35 \times 10^8 \text{ cm}^{-1}, \\ \chi'_{0e} &= -0.15 \times 10^{-4}, & \chi''_{0e} &= 0.69 \times 10^{-6}, \\ \chi'_{ge} &= -0.10 \times 10^{-4}, & \chi''_{ge} &= 0.67 \times 10^{-6}. \end{aligned} \quad (13)$$

The α -iron crystal has cubic crystalline structure with interplanes distance $d = 2.87 \times 10^{-8}$ cm. In addition, we assume it to be enriched to 90% with the resonant Mössbauer isotope $^{57}_{26}\text{Fe}$, which has the natural decay width $\Gamma = 4.66 \times 10^{-12}$ keV. The coefficient of internal conversion $\alpha_C = 8.56$ and the structure factor $S(\mathbf{g}) = 2$ for $^{57}_{26}\text{Fe}$.

For CsF, we employ the (111) reflection with the parameters³⁴

$$\begin{aligned} \hbar\omega_B &= 80.997 \text{ keV}, & k_0 &= 4.10 \times 10^9 \text{ cm}^{-1}, \\ \chi'_{0e} &= -0.25 \times 10^{-6}, & \chi''_{0e} &= 0.42 \times 10^{-8}, \\ \chi'_{ge} &= -0.15 \times 10^{-6}, & \chi''_{ge} &= 0.39 \times 10^{-8}. \end{aligned} \quad (14)$$

The CsF crystal has a cubic crystalline structure with interplanar distance $d = 6.008 \times 10^{-8}$ cm. The natural decay width of the $^{133}_{55}\text{Cs}$ isotope is $\Gamma = 72.77 \times 10^{-12}$ keV, the internal conversion coefficient $\alpha_C = 1.72$, and the structure factor $S(\mathbf{g}) = 4$.

For InSb, we employ the (222) reflection with the parameters³⁴

$$\begin{aligned} \hbar\omega_B &= 37.133 \text{ keV}, & k_0 &= 1.88 \times 10^9 \text{ cm}^{-1}, \\ \chi'_{0e} &= -0.15 \times 10^{-5}, & \chi''_{0e} &= 0.72 \times 10^{-7}, \\ \chi'_{ge} &= 0.17 \times 10^{-7}, & \chi''_{ge} &= -0.46 \times 10^{-8}. \end{aligned} \quad (15)$$

The CsF crystal has cubic crystalline structure with interplanar distance $d = 6.4789 \times 10^{-8}$ cm. The isotope $^{121}_{51}\text{Sb}$ has a natural decay width $\Gamma = 0.13 \times 10^{-6}$ eV, the internal conversion coefficient $\alpha_C = 11.11$. The structure factors are $S(\mathbf{g}) = -4$ for $^{121}_{51}\text{Sb}$ and $S(\mathbf{g}) = 4$ for ^{49}In .

Crystal	θ_0	ϕ_0	ψ_0
α -iron	107.468	-162.532	107.468
CsF	91.46	-177.94	91.55
InSb	95.91	-171.62	96.28

Table I. The angles θ_0 , ϕ_0 of a spherical coordinate system together with the angle ψ_0 , which determine the direction of emission and the orientation of the crystal with respect to the particle velocity (see Fig. 1).

Regarding the electron bunch parameters, we have investigated two accelerator facilities, namely Spring-8²⁹ with electron beam energy 8000 MeV, and ESRF³⁰ with electron beam energy 6030 MeV. The Spring-8 facility provides electron beams with natural vertical emittance $\epsilon = 6.8 \times 10^{-10} \text{ cm} \times \text{rad}$, while the ESRF facility has a vertical emittance $\epsilon = 2.5 \times 10^{-9} \text{ cm} \times \text{rad}$. For all simulations, the angular spread in the horizontal y -direction $\Delta\theta_{ey}$ was taken to be 10^{-3} rad.

Direction and divergence of the X-ray emission. Table I summarizes the angles characterizing the vector \mathbf{k} which determines the X-ray emission direction. The actual emission is happening in the direction $\mathbf{k}' = -\mathbf{k}$. Possible values for the angles ϕ_0 , ψ_0 range from $-\pi$ to π , and values for the angle θ_0 range from 0 to π . In the angular distribution of the emitted radiation shown in Fig. 4, two qualitatively different scales can be observed. A narrower first scale arises from the Cherenkov radiation condition. It is satisfied exactly at $q' = 0$. In this case, the angular width is defined through the coherent length L_g and the width of $q' \sim (k_0 L_g)^{-1} \sim 10^{-8}$. The second direction, which is perpendicular to q' is characterized via a variable p' . This variable is associated to the maximum of the diffracted wave, and is of the order $p' \sim \sqrt{|\chi_0''|} \sim 10^{-3}$. Consequently, the PMR is concentrated around the direction given by the vector $\mathbf{k}'_0 = -\mathbf{k}_0 = (g_x + \omega_0/v, g_y, g_z)$.

Due to the finite crystal size ~ 1 mm, the beam of PMR seen by the detector has at least a width given by the crystal size, projected onto the plane defined by the vector normal to the detector. The beam divergence is of order $\Delta\Omega \approx 10^{-3} \times 10^{-8} \text{ rad}^2$ is defined via the angular divergence of the emitted gamma quanta ($\approx \gamma^{-1}$). Therefore, the target and detector should ideally be comparable or larger than the crystal size.

Calculation of the absorption spectrum. The absorption spectrum is computed as

$$N(\omega_s) = N_e \int \left(\frac{I(\omega) + I(-\omega)}{2} - I_B \right) \times e^{-k_0 D |\text{Im} \chi_0(\omega - \omega_s)|} d\omega, \quad (16)$$

where I_B is the electronic part of the intensity and $\chi_0(\omega - \omega_s)$ includes both the electronic and the nuclear polarizabilities. Here N_e is the number of electrons per second.

[†] Corresponding author: ilya.feranchuk@tdtu.edu.vn

- [1] R. Röhlsberger, *Nuclear Condensed Matter Physics with Synchrotron Radiation*, edited by G. Höhler, J. H. Kühn, T. Müller, J. Trümper, A. Ruckenstein, P. Wölffe, and F. Steiner, Springer Tracts in Modern Physics, Vol. 208 (Springer Berlin Heidelberg, Berlin, Heidelberg, 2005).
- [2] M. Kalvius and P. Kienle, eds., *The Rudolf Mössbauer Story* (Springer Berlin Heidelberg, Berlin, Heidelberg, 2012).
- [3] R. Ruffer and A. I. Chumakov, in *Synchrotron Light Sources and Free-Electron Lasers*, edited by E. J. Jaeschke, S. Khan, J. R. Schneider, and J. B. Hastings (Springer International Publishing, Cham, 2016) pp. 1759–1795.
- [4] B. Adams, G. Aeppli, T. Allison, A. Q. R. Baron, P. Bucksbaum, A. I. Chumakov, C. Corder, S. P. Cramer, S. DeBeer, Y. Ding, J. Evers, J. Frisch, M. Fuchs, G. Grübel, J. B. Hastings, C. M. Heyl, L. Holberg, Z. Huang, T. Ishikawa, A. Kaldun, K.-J. Kim, T. Kolodziej, J. Krzywinski, Z. Li, W.-T. Liao, R. Lindberg, A. Madsen, T. Maxwell, G. Monaco, K. Nelson, A. Pálffy, G. Porat, W. Qin, T. Raubenheimer, D. A. Reis, R. Röhlsberger, R. Santra, R. Schoenlein, V. Schünemann, O. Shpyrko, Y. Shvyd'ko, S. Shwartz, A. Singer, S. K. Sinha, M. Sutton, K. Tamasaku, H.-C. Wille, M. Yabashi, J. Ye, and D. Zhu, [arXiv:1903.09317 \[physics\]](https://arxiv.org/abs/1903.09317) (2019), arXiv: 1903.09317.
- [5] K. P. Heeg, A. Kaldun, C. Strohm, P. Reiser, C. Ott, R. Subramanian, D. Lentrodt, J. Haber, H.-C. Wille, S. Goerttler, R. Ruffer, C. H. Keitel, R. Röhlsberger, T. Pfeifer, and J. Evers, *Science* **357**, 375 (2017).
- [6] A. Q. R. Baron, [arXiv:1504.01098 \[cond-mat\]](https://arxiv.org/abs/1504.01098) (2015), arXiv: 1504.01098.
- [7] B. W. Adams, C. Buth, S. M. Cavaletto, J. Evers, Z. Harman, C. H. Keitel, A. Pálffy, A. Picón, R. Röhlsberger, Y. Rostovtsev, and K. Tamasaku, *Journal of Modern Optics* **60**, 2 (2013).
- [8] R. Röhlsberger, J. Evers, and S. Shwartz, in *Synchrotron Light Sources and Free-Electron Lasers*, edited by E. J. Jaeschke, S. Khan, J. R. Schneider, and J. B. Hastings (Springer International Publishing, Cham, 2016) pp. 1197–1229.
- [9] E. Kuznetsova and O. Kocharovskaya, *Nature Photonics* **11**, 685 (2017).
- [10] P. Alexeev, O. Leupold, I. Sergueev, M. Herlitschke, D. F. McMorrow, R. S. Perry, E. C. Hunter, R. Röhlsberger, and H.-C. Wille, *Scientific Reports* **9** (2019), 10.1038/s41598-019-41130-3.
- [11] S. L. Ruby, *Le Journal de Physique Colloques* **35**, C6 (1974).
- [12] E. Gerda, R. Ruffer, H. Winkler, W. Tolksdorf, C. P. Klages, and J. P. Hannon, *Physical Review Letters* **54**, 835 (1985).
- [13] G. V. Smirnov, U. van Bürck, A. I. Chumakov, A. Q. R. Baron, and R. Ruffer, *Phys. Rev. B* **55**, 5811 (1997).
- [14] R. Masuda, T. Mitsui, S. Kitao, S. Higashitaniguchi, Y. Yoda, and M. Seto, *Japanese Journal of Applied Physics* **47**, 8087 (2008).
- [15] M. Seto, R. Masuda, S. Higashitaniguchi, S. Kitao, Y. Kobayashi, C. Inaba, T. Mitsui, and Y. Yoda, *Phys. Rev. Lett.* **102**, 217602 (2009).
- [16] V. Potapkin, A. I. Chumakov, G. V. Smirnov, J.-P. Celse, R. Ruffer, C. McCammon, and L. Dubrovinsky, *Journal of Synchrotron Radiation* **19**, 559 (2012).
- [17] V. G. Baryshevsky, I. D. Feranchuk, and A. P. Ulyanenko, *Parametric X-Ray Radiation in Crystals: Theory, Experiment and Applications (Springer Tracts in Modern Physics)* (Springer, 2006).
- [18] V. G. Baryshevsky, I. D. Feranchuk, A. O. Grubich, and A. V. Ivashin, *Nuclear Instruments and Methods in Physics Research Section A: Accelerators, Spectrometers, Detectors and Associated Equipment* **249**, 306 (1986).

* olegskor@gmail.com

- [19] I. D. Feranchuk and A. V. Ivashin, *J. Phys. France* **46**, 1981 (1985).
- [20] K. H. Brenzinger, C. Herberg, B. Limburg, H. Backe, S. Dambach, H. Euteneuer, F. Hagenbuck, H. Hartmann, K. Johann, K. H. Kaiser, O. Kettig, G. Knies, G. Kube, W. Lauth, H. Schöpe, and T. Walcher, *Zeitschrift für Physik A Hadrons and Nuclei* **358**, 107 (1997).
- [21] K.-H. Brenzinger, B. Limburg, H. Backe, S. Dambach, H. Euteneuer, F. Hagenbuck, C. Herberg, K. H. Kaiser, O. Kettig, G. Kube, W. Lauth, H. Schöpe, and T. Walcher, *Phys. Rev. Lett.* **79**, 2462 (1997).
- [22] J. Hyun, M. Satoh, M. Yoshida, T. Sakai, Y. Hayakawa, T. Tanaka, K. Hayakawa, I. Sato, and K. Endo, *Phys. Rev. Accel. Beams* **21**, 014701 (2018).
- [23] A. Ahmadi and I. D. Feranchuk, *The European Physical Journal Applied Physics* **62**, 10702 (2013).
- [24] A. Ahmadi and I. D. Feranchuk, *Nuclear Instruments and Methods in Physics Research Section B: Beam Interactions with Materials and Atoms* **311**, 78 (2013).
- [25] O. D. Skoromnik, V. G. Baryshevsky, A. P. Ulyanenko, and I. D. Feranchuk, *Nuclear Instruments and Methods in Physics Research Section B: Beam Interactions with Materials and Atoms* **412**, 86 (2017).
- [26] A. Authier, *Dynamical Theory of X-ray Diffraction*, International Union of Crystallography monographs on crystallography (Oxford University Press, 2001).
- [27] O. D. Skoromnik, I. D. Feranchuk, and D. V. Lu, *Nuclear Instruments and Methods in Physics Research Section B: Beam Interactions with Materials and Atoms* **444**, 125 (2019).
- [28] A. M. Afanas'ev and Y. Kagan, *Soviet Physics JETP* **21**, 215 (1965).
- [29] Spring-8 authors, "Spring-8 synchrotrone facility. Parameters," http://www.spring8.or.jp/pdf/en/res_fro/05/185-188.pdf, accessed: 07-03-2019.
- [30] ESRF authors, "ESRF synchrotrone facility. Parameters," <https://www.esrf.eu/home/UsersAndScience/Accelerators/parameters.html>, accessed: 07-03-2019.
- [31] M. Born and E. Wolf, *Principles of Optics: Electromagnetic Theory of Propagation, Interference and Diffraction of Light* (Elsevier Science, 2013).
- [32] M. Ter-Mikaelian, *High-energy electromagnetic processes in condensed media*, Interscience tracts on physics and astronomy (Wiley-Interscience, 1972).
- [33] M. Tanabashi, K. Hagiwara, K. Hikasa, K. Nakamura, Y. Sumino, F. Takahashi, J. Tanaka, K. Agashe, G. Aielli, C. Amsler, M. Antonelli, D. M. Asner, H. Baer, S. Banerjee, R. M. Barnett, T. Basaglia, C. W. Bauer, J. J. Beatty, V. I. Belousov, J. Beringer, S. Bethke, A. Bettini, H. Bichsel, O. Biebel, K. M. Black, E. Blucher, O. Buchmuller, V. Burkert, M. A. Bychkov, R. N. Cahn, M. Carena, A. Ceccucci, A. Cerri, D. Chakraborty, M.-C. Chen, R. S. Chivukula, G. Cowan, O. Dahl, G. D'Ambrosio, T. Damour, D. de Florian, A. de Gouvêa, T. DeGrand, P. de Jong, G. Dissertori, B. A. Dobrescu, M. D'Onofrio, M. Doser, M. Drees, H. K. Dreiner, D. A. Dwyer, P. Eerola, S. Eidelman, J. Ellis, J. Erler, V. V. Ezhela, W. Fetscher, B. D. Fields, R. Firestone, B. Foster, A. Freitas, H. Gallagher, L. Garren, H.-J. Gerber, G. Gerbier, T. Gershon, Y. Gershtein, T. Gherghetta, A. A. Godizov, M. Goodman, C. Grab, A. V. Gritsan, C. Grojean, D. E. Groom, M. Grünewald, A. Gurtu, T. Gutsche, H. E. Haber, C. Hanhart, S. Hashimoto, Y. Hayato, K. G. Hayes, A. Hebecker, S. Heinemeyer, B. Heltsley, J. J. Hernández-Rey, J. Hisano, A. Höcker, J. Holder, A. Holtkamp, T. Hyodo, K. D. Irwin, K. F. Johnson, M. Kado, M. Karliner, U. F. Katz, S. R. Klein, E. Klempt, R. V. Kowalewski, F. Krauss, M. Kreps, B. Krusche, Y. V. Kuyanov, Y. Kwon, O. Lahav, J. Laiho, J. Lesgourgues, A. Liddle, Z. Ligeti, C.-J. Lin, C. Lippmann, T. M. Liss, L. Littenberg, K. S. Lugovsky, S. B. Lugovsky, A. Lusiani, Y. Makida, F. Maltoni, T. Mannel, A. V. Manohar, W. J. Marciano, A. D. Martin, A. Masoni, J. Matthews, U.-G. Meißner, D. Milstead, R. E. Mitchell, K. Mönig, P. Molaro, F. Moortgat, M. Moskvic, H. Murayama, M. Narain, P. Nason, S. Navas, M. Neubert, P. Nevski, Y. Nir, K. A. Olive, S. Pagan Griso, J. Parsons, C. Patrignani, J. A. Peacock, M. Pennington, S. T. Petcov, V. A. Petrov, E. Pianori, A. Piepke, A. Pomarol, A. Quadt, J. Rademacker, G. Raffelt, B. N. Ratcliff, P. Richardson, A. Ringwald, S. Roesler, S. Rolli, A. Romaniouk, L. J. Rosenberg, J. L. Rosner, G. Rybka, R. A. Ryutin, C. T. Sachrajda, Y. Sakai, G. P. Salam, S. Sarkar, F. Sauli, O. Schneider, K. Scholberg, A. J. Schwartz, D. Scott, V. Sharma, S. R. Sharpe, T. Shutt, M. Silari, T. Sjöstrand, P. Skands, T. Skwarnicki, J. G. Smith, G. F. Smoot, S. Spanier, H. Spieler, C. Spiering, A. Stahl, S. L. Stone, T. Sumiyoshi, M. J. Syphers, K. Terashi, J. Terning, U. Thoma, R. S. Thorne, L. Tiator, M. Titov, N. P. Tkachenko, N. A. Törnqvist, D. R. Tovey, G. Valencia, R. Van de Water, N. Varelas, G. Venanzoni, L. Verde, M. G. Vincet, P. Vogel, A. Vogt, S. P. Wakely, W. Walkowiak, C. W. Walter, D. Wands, D. R. Ward, M. O. Wascko, G. Weiglein, D. H. Weinberg, E. J. Weinberg, M. White, L. R. Wiencke, S. Willocq, C. G. Wohl, J. Womersley, C. L. Woody, R. L. Workman, W.-M. Yao, G. P. Zeller, O. V. Zenin, R.-Y. Zhu, S.-L. Zhu, F. Zimmermann, P. A. Zyla, J. Anderson, L. Fuller, V. S. Lugovsky, and P. Schaffner (Particle Data Group), *Phys. Rev. D* **98**, 030001 (2018).
- [34] S. A. Stepanov, "X-ray dynamical diffraction web server," <http://x-server.gmca.aps.anl.gov/>, accessed: 07-03-2019.